Lawrence Berkeley Laboratory
UNIVERSITY OF CALIFORNIA

Materials & Molecular Research Division

Submitted to Journal of Metals

RECENT TEM APPLICATIONS

D.A. Ackland, U. Dahmen, C.J. Echer, R. Kilaas,
K.M. Krishnan, C. Nelson, M.A. O'Keefe,
W. Smith, and J. Turner

October 1986

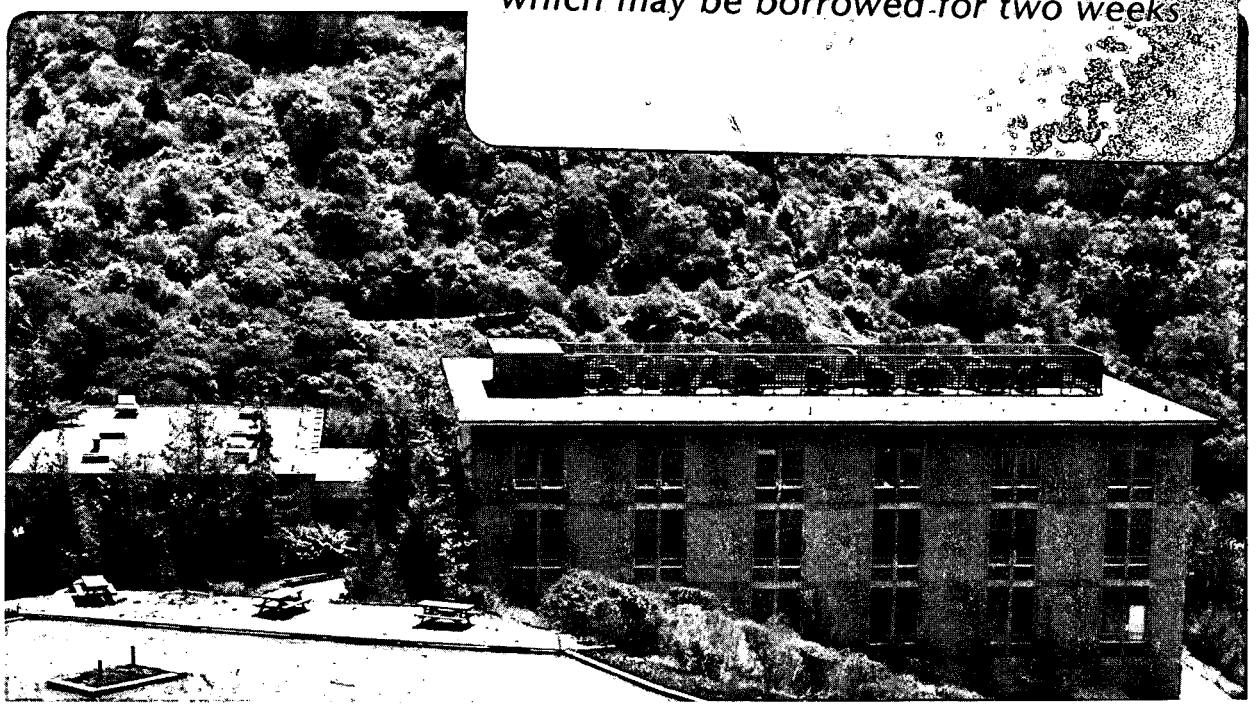

Prepared for the U.S. Department of Energy under Contract DE-AC03-76SF00098

DISCLAIMER

RECENT TEM APPLICATIONS

D.A. Ackland, U. Dahmen, C.J. Echer, R. Kilaas, K.M. Krishnan,
C. Nelson, M.A. O'Keefe, W. Smith, J. Turner

Lawrence Berkeley Laboratory
University of California
Berkeley, California 94720

This paper describes the conceptual basis for the systems design and new equipment integration at Lawrence Berkeley Laboratory's National Center for Electron Microscopy. Computer aided image processing helps scientists develop better structural models which, in turn, help define new directions for improved image processing. Several examples are cited to demonstrate how improvements in experimental techniques, high voltage, high resolution and microanalytical capabilities, combined with computer processing, impact on materials characterization.

INTRODUCTION

Over the last ten years, regional and national electron microscopy centers have been established to provide the U.S. scientific community with unique capabilities for the in-depth microstructural characterization of materials. Although they function independently, each facility offers complementary instrumentation and strengths. At Berkeley's National Center for Electron Microscopy (NCEM)[1], increased emphasis is being placed on using the various microscopes and supporting functions in an integrated manner. Typically, an in-situ treatment in a high voltage electron microscope (HVEM) will be preceded or followed by high resolution imaging in an atomic resolution microscope (ARM) or by microchemical analysis in an analytical electron microscope (AEM), with each function strongly supported by the developing computer facility.

The centerpiece of the facility is a JEOL-ARM-1000 atomic resolution microscope which has been specifically designed for and dedicated to superior performance in the high resolution imaging mode. Proven point-to-point resolution of~0.15nm has been achieved and its combination of resolution performance and specimen tilting capabilities (±40° biaxial) is unique. By incorporating a microprocessor-controlled height (Z)-variable goniometer, the microscope operates with a constant $C_S\lambda$ product over its entire voltage range (400kV to 1000kV). At higher lens excitation values, the microscope can be run in condenser-objective mode, enabling convergent beam electron diffraction (CBED) patterns to be taken from the same specimen areas imaged in high resolution. For increased mechanical stability, the top entry stage configuration is used. The microscope uses LaB_6 filaments and a unique viewing glass for additional brightness. It is presently being equipped with a computer-linked video system for real-time image analysis. This ARM microscope is the basis for the now popular commercial JEOL 400 kV microscope with point-to-point resolution of 0.17 nm.

A second HVEM, a Kratos EM-1500, was designed primarily for dynamic in-situ studies but it can also resolve structures at the 0.3nm level. It is the first electron microscope to be built by Kratos with a maximum acceleration voltage of 1.5 MV. As such, it provides accelerating voltages in the range 1200-1500kV not available elsewhere in the U.S. The voltage can be varied continuously for critical voltage or convergent beam diffraction studies. The accelerator vacuum allows use of LaB_6 filaments. The microscope features both a top-entry stage for high resolution studies, and a side-entry stage for general, dynamic in-situ, and environmental cell studies.

A JEOL 200CX AEM at NCEM provides state-of-the-art microanalytical capabilities built around a KEVEX System 8000 with a DEC LSI 11/73 computer. It is configured to run standard quantification and imaging software while maintaining the capabilitiy of program development for more sophisticated applications. The systems's hardware includes a high angle energy dispersive X-ray detector with a resolution of 155eV for MnK α, an ultra-thin window EDX detector capable of detecting all elements with $Z \geq 6$; and a Gatan 607 electron energy loss spectrometer capable of routinely achieving 2eV resolution.

A COMPUTER SYSTEM FOR IMAGE ANALYSIS

To obtain all possible information contained in an image (or series of images), two complementary techniques of image analysis are employed. First, image processing can be used to reduce noise in electron micrographs by spatial averaging. The technique combines different spatial frequency pass-bands present in a through-focus series of micrographs[2,3] for a higher overall resolution than present in any single micrograph in the series. The system eventually determines the complex amplitude (modulus and phase) of the electron wave leaving the exit surface of the specimen. Second, image simulation can be used to produce a representation of the electron microscope image under specified conditions. Direct comparison with the experimental micrograph then allows assessment of the validity of the model used to represent the specimen structure. The two techniques are symbiotic, providing valuable feedback information to one another.

The image analysis facility at the NCEM requires that a system be easy to use by outside clients, yet still be sophisticated enough to allow continual upgrading with the latest imaging algorithms and programming techniques. Available image simulation packages like SHRLI

[4,5] are written for general computer systems and require only a minimum of standard software and hardware (a Fortran compiler and a lineprinter capable of overprinting). A new system-dependent image simulation package was written based on experience with programs at Berkeley [6] and with SHRLI. For image processing the SEMPER package [7] was chosen, as this suite of programs can be modified to take advantage of any special hardware available.

The system hardware is similar to that used in the image processing system described in Ref. 7. The host is a microVAX II computer with 7MB of memory, a 71MB Winchester disk (RD53) for storage of program and operating system files. Data storage (mostly images) is provided by a 503MB Winchester disk (QDA50/61), with backup onto 9-track tape. Both the simulated and processed images are displayed with a two-user Gould IP9527 which has the ability to display an area of 1024 x 1024 pixels (picture elements) at each of two work-stations. A 16MB memory shared between the two stations yields a maximum image size of 4096 x 4096 when only one station is in use. In addition to its display function, the IP9527 has the ability to process images, display their intensity histograms, and "warp" them to correct for any distortion. These functions are interactively controlled by means of the steerable cursor. For image processing, SEMPER takes advantage of this interactivity to enable the quick definition of lattices in both real and reciprocal space, and to adjust image magnifications for on-screen comparisons of processed and simulated images. For image simulation, the new package (named CEMPAS for Center for Electron Microscopy Processing And Simulation) also provides an interactive milieu via a mouse input. A CEMPAS menu can be used to create atom position files,

view the crystal unit cell from any specified direction, simulate the dynamical diffraction process for any specimen thickness or tilt, and image the resultant simulated electron wavefield under any selected microscope conditions. In addition, it is possible to use the mouse to select commands from a menu in order to display simulated electron diffraction patterns and diffractograms. Similarly, it is easy to display plots of CTF's (linear-image Contrast Transfer Functions) and plots of variation in diffracted beam intensities with specimen thickness. Diffraction (multislice) calculations using the attached CSPI MM+4 array processor require only a few minutes' time. Several hours would otherwise be required when using the microVAX alone.

The simulation process commences with the formation of a model of the structure. Figure 1a shows a display of a model of the δ_1 phase of the ceramic $Y_2Si_2O_7$ in [100] orientation [8]. Here the atoms are drawn as shaded spheres of radius proportional to their covalent radii. Figure 1b shows the best match of a simulation from this model with a micrograph obtained on the atomic resolution microscope.

In addition to the image processing computer, a second system has been designed to acquire and enhance electron microscope images in real time at video rates. This real-time system uses another microVAX II host computer linked to the main host via ethernet connectors, with a grabber/enhancer for each electron microscope consisting of three VME cards (DataCube Max-Video) in a VME-bus backplane. Each grabber/enhancer has the ability to digitize images at video rates, time-average the image signal to reduce noise, store/display the image, and adjust its contrast. A small array processor (Mercury ZIP3232 with 2MB memory) present on the VME-bus, provides the microscope operator with diffractograms of real-time images with a 1.5 second lag-time.

PRECIPITATION IN AN Al-Ge ALLOY

The unusual variety of germanium precipitate shapes and orientation relationships observed in quenched and aged Al-Ge alloys reflects the difficulty of nucleating and growing a diamond-cubic precipitate in a face-centered cubic matrix. In addition, accommodation of the 36% volume increase necessitates vacancies for the precipitation reaction to proceed at all. Precipitate-free zones are therefore found near vacancy sinks such as surfaces and grain boundaries. An example is shown in Fig. 2a, which illustrates the high density of precipitates in the grain interiors and their absence in a uniform 0.5 μm wide vacancy-depleted zone near the boundary. In this low-magnification view of a relatively thick foil the precipitate morphology cannot be distinguished. At higher magnification and in thinner foils (Fig. 2b) most particles are needle shaped after aging one hour at 240° C. Crystallographic analysis revealed that the majority of the needles lie in $\langle 100 \rangle_{Al}$ directions, although $\langle 110 \rangle_{Al}$ needles were also found. The tilting and resolution capability of the ARM allowed high-resolution observations to be made on a large number of particles by viewing them along their needle axis. Even though only needles along $\langle 110 \rangle_{Ge} \,||\, \langle 100 \rangle_{Al}$ were examined, a fascinating variety of cross-section morphologies, internal and interface structures and orientation relationships were observed. Within the confines of $\langle 110 \rangle_{Ge} \,||\, \langle 100 \rangle_{Al}$ three primary orientation relationships were observed[9-11]:

(a) $\{111\}_{Ge} \,||\, \{100\}_{Al}$

(b) $\{100\}_{Ge} \,||\, \{100\}_{Al}$ and

(c) $\{110\}_{Ge} \,||\, \{110\}_{Al}$

An example of a typical precipitate cross-section is shown in Fig. 2c. The two long flat facets are $\{111\}_{Ge}$ planes parallel to $\{310\}_{Al}$ while the shorter facets are another set of $\{111\}_{Ge}$ planes parallel to $\{100\}_{Al}$. The orientation relationship of this precipitate and the one most frequently found is that given in relationship (a) with monoclinic 2/m symmetry. The shape of this particle also has approximately 2/m symmetry along its axis, but the perfect symmetry is disrupted by the internal twins labelled 1,2 and 3. The central precipitate and its twin 1 have the same (a) orientation relationship because they are mirror-related across the {100} symmetry plane of the matrix. On the other hand, twins 2 and 3 are in a different (secondary) orientation relationship because their twin plane is the {111} Ge plane that is parallel to {310} Al. The corresponding interfaces with the matrix are atomically flat on the Ge side, leading to a stepped appearance on the Al side. Closer examination reveals an apparent stacking fault in the Ge layer next to this interface. Further high-resolution microscopy, especially comparison with other morphologies in the same alloy, is expected to provide additional clues on how these particles grow and how they are accommodated in the matrix.

COMPOSITION OF THE ICOSAHEDRAL PHASE IN QUASICRYSTALLINE Al-Mn ALLOYS

The existence of a metallic solid with long-range orientational order and an icosahedral point group inconsistent with lattice translations in rapidly solidified samples of aluminum alloyed with manganese has been widely reported [12,13] based on electron diffraction measurements. The interpretation of these diffraction patterns using a multiple twinning model [14] has been shown to be inconsistent with

experimental observations [15,16]. However, the point group of this phase has been conclusively shown to be icosahedral $m\bar{3}\bar{5}$ by convergent beam electron diffraction [17] and a typical pattern taken along a five-fold axis is shown in Fig. 3a. There are no published theories that satisfactorily explain these experimental observations [18,19]. Recently, Katz and Duneau [20] and independently, Elser [21] have computed the diffraction pattern of a three-dimensional Penrose pattern using an elegant projection scheme from a six-dimensional periodic lattice. They find δ-function peaks that are dense in reciprocal space, where the most intense peak positions not only accurately match the experimental diffraction patterns but also exhibit the same scaling relationships. However, an understanding of the peak intensities is as yet non-existent since it entails a detailed knowledge of the aluminum and manganese atom positions in the quasilattice. To solve this problem it is first necessary to determine the composition of the icosahedral phase as accurately as possible.

Figure 3b illustrates the two-phase microstructure containing the quasicrystalline icosahedral phase in a sample of starting composition Al - 25.3 wt%Mn prepared by arc melting and splat quenching (hammer and anvil) with cooling rates of 10^{6-7}°C/s [22]. Its composition has been determined at high spatial resolution by energy dispersive X-ray microanalysis using convergent probes of 200nm diameter. A homogeneous reference standard alloy of composition Al-3.5 wt%Mn was prepared and the experimental Cliff-Lorimer factor, $K_{Mn,Al}$ was determined to be 0.92 ± 0.04 [23]. The composition of the icosahedral phase and the aluminum-rich matrix phase in this alloy were determined for a large number of samples.

Typical EDX spectra from spatially resolved regions of the sample, given in Figs. 3c and d, show an Al to Mn ratio of 4 to 1 in the quasicrystals. However, more recent experiments [24] point to a wide range of compositions for the icosahedral phase depending on the starting composition of the binary alloy. Efforts to determine the metastable phase diagram are now in progress.

IMPROVED PHOTOGRAPHIC PROCESS FOR CONVERGENT BEAM ELECTRON DIFFRACTION

It is well recognized that the use of the conventional D-19 (Kodak Tradename) process to develop photographic negatives used in transmission electron microscopes for convergent beam electron diffraction applications suffers from two inherent limitations: the wide intensity range in the actual electron exposure and the narrow latitude of film development. Further, the exposure meters in commercial microscopes are unreliable for these applications. Hence it is necessary to estimate the required exposure accurately, as this conventional process is very sensitive to incorrect exposure and allows little room for correction once the exposed film is developed.

The use of a surface developer, pyrocatechol, to process transmission electron microscope negatives has been shown to have significant advantages [25]. The process, developed at NCEM, is tolerant of a large margin of error in the electron exposure, produces a negative that not only retains details in both the highlight as well as the faint regions but also preserves local contrast, is relatively easy to print, has a large development time latitude and can be developed under safe-light conditions. Improved acuteness and an enhanced signal

to noise ratio due to prolonged exposures associated with this process have also been observed. Typical results using this process (Figure 4) are very encouraging. In fact, the improved resolution inherent in this image should shed some light on the controversial question of the space group of spinels [26].

HIGH RESOLUTION STUDY OF ALUMINUM OXIDATION

Although extensively studied for many years (27-30), the oxidation of aluminum still defies complete description, primarily due to a lack of resolution in experimental studies. NCEM conducted research on this topic [31] by utilizing facilities for high resolution electron microscopy. Samples were obtained by oxidizing 99.999% pure aluminum in 1 atm air at either 550°C or 600°C for times ranging from one-half hour to 4 weeks. To image the interfacial region in detail, cross-sectional specimens were prepared by forming an oxide-to-oxide laminate with epoxy, followed by mechanical polishing and then argon ion milling. The featured images were recorded in a <110> oxide zone axis orientation using a JEOL 200CX microscope with ultrahigh resolution goniometer at 200 kV.

As seen in Fig. 5a, the aluminum interface with the high temperature oxide is highly crystallographic, sharply faceted, and coherent, in this case maintaining perfectly parallel orientation between unit cells of both phases. The oxide phase is γ-Al_2O_3, identified by its lattice spacings, and the interfacial plane is always found to be a {111} octahedral plane of this phase. Its lattice correspondence shows that the aluminum transforms to the oxide structure by atomic shuffling and absorbing vacancies for a portion of the Al sites in the unit cell

of the $\Sigma = 1$ Coincidence Site Lattice (CSL), accompanied by a small (7%) volume contraction. It is also clear from this image that growth is facilitated by ledges on the close-packed planes of the merging oxide. However, the crystalline oxide does not always maintain a perfect structure. Figure 5b shows the atomic nature of the twinned variants of the γ phase meeting at a $\Sigma = 3$ CSL orientation (confirmed by theinset image simulations). This was found to be a common morphology. The polycrystalline oxide islands were, in fact, multiply-twinned over their entire volume. Oxidation promotes such twinning by the volume constraint and faceted growth front associated with the solid state reaction.

Other results point to the mechanisms of oxide nucleation at the low temperature amorphous oxide interface. The study also delineated the differences between parallel and twin orientations at the crystalline oxide/aluminum matrix interface, and suggested atomic models for the development of the oxide phase in all of its variants. These results will appear in future publications [32].

IN-SITU STRAINING EXPERIMENTS

A recent addition to the selection of stages available for in-situ experiments on the 1500kV high voltage microscope is a double tilt Birmingham-type straining stage with combined mechanical and piezoelectric drive. It enables direct observation of slip propagation as the mini-tensile sample is strained at a controlled rate. Events can be recorded on video tape for detailed frame-by-frame analysis. An example of a straining sequence in a polycrystalline stainless steel sample from the work of Ohio State University researcher W.A.T. Clark is shown in Fig. 6. In the first two frames (Figs. 6a and b) dislocation

slip bands are seen to approach the boundary causing an increasing stress concentration, which is made visible through strain-lobe contrast at two different pile-ups in Fig. 6c. From observations such as these it is possible to deduce micromechanisms of slip propagation. When used in conjunction with a detailed contrast analysis it will be possible to determine the boundary orientation, the dislocation Burgers vectors, line directions and positions. These experimental parameters can be used to calculate the local stress field and to identify the fundamental mechanisms of slip propagation across grain boundaries.

ACKNOWLEDGEMENTS

The National Center for Electron Microscopy and the research reported here are supported by the Director, Office of Energy Research, Office of Basic Energy Sciences, Materials Science Division, U.S. Department of Energy under Contract No. DE-AC03-76SF00098.

REFERENCES

[1] R. Gronsky, G. Thomas and K.H. Westmacott, J. Metals 37, (1985), 36.

[2] P. Schiske, in Image Processing and Computer-aided design in Electron Optics, P.W. Hawkes (ed.) Academic, London (1973) 82-90.

[3] E.J. Kirkland, in Proc. 42nd EMSA, G.W. Bailey (ed.) San Francisco Press, San Francisco (1984) 432-433.

[4] M.A. O'Keefe, P.R. Buseck and S. Ijima, Nature 274, (1978) 322-324.

[5] M.A. O'Keefe, in Electron Optical Systems, J.J. Hren et al. (eds.) SEM Inc., AMF O'Hare (1984) 209-220.

[6] R. Kilaas, Ph.D. thesis, University of California, Berkeley (1985).

[7] W.O. Saxton, in Inst. Phys. Conf. Ser. No. 44, Institute of Physics, London (1979) 78-87.

[8] R.S. Rai, T.R. Dinger, G.Thomas, Proc. EMSA (1986), p. 444.

[9] U. Köster, Ph.D. Thesis, Göttingen (1971).

[10] U. Dahmen and K.H. Westmacott, Proc. MRS Symposium on Materials Problem Solving with the TEM, L. Hobbs, D.B. Williams, K.H. Westmacott, eds., Boston (1985), in press.

[11] U. Dahmen and K.H. Westmacott, Science, 233 (1986), 875.

[12] D. Schechtman and I.A. Blech, Met. Trans. 16A, 1005 (1985).

[13] D. Schechtman, I.A. Blech, D. Gratias and J.W. Cahn, Phys. Rev. Lett. 53, 1951 (1985).

[14] R.D. Field and H.L. Frazer, Mat. Sci. Eng. 68, L17 (1984-85).

[15] R. Gronsky, K.M. Krishnan and L.E. Tanner, Proc. 43rd Annual EMSA Meeting, Louisville, Kentucky, p. 34 (1985).

[16] D. Schechtman, D. Gratias and J.W. Cahn, C.R. Acad. Sci. Paris 18, 909 (1985).

[17] L.A. Bendersky and M.J. Kaufman, submitted to Phil. Mag. Lett. (1985).

[18] D.R. Nelson and B.I. Halperin, Science, 229, 233 (1985).

[19] A.L. Mackay and P. Kramer, Nature 316, 17 (1985).

[20] M. Duneau and A. Katz, Phys. Rev. Lett. 54, 2688 (1985).

[21] V. Elser, AT & T and Bell Labs. Preprint, (1986).

[22] L.E. Tanner and R. Ray, Acta Met. 27, 1727 (1979).

[23] K.M. Krishnan, R. Gronsky and L.E. Tanner, Scripta Met. 20, 239 (1986).

[24] K.M. Krishnan, unpublished results.

[25] J.H. Turner and K.M. Krishnan, J. Elec. Mic. Tech., in press.

[26] B.C. DeCooman and C.B. Carter, Phil. Mag. 51, 175 (1985).

[27] M.S. Hunter and P. Fowle, J. Electrochem. Soc., 103, 482 (1956).

[28] R.S. Goodrich, Jr. and G.S. Ansell, Trans. Met. Soc. AIME, 230, 1372 (1964).

[29] G.M. Scamans and E.P. Butler, Met. Trans. A., 6A, 2055 (1975).

[30] K. Wefers, Aluminum, 57, 722 (1981).

[31] J.Y. Lee, Ph.D. Thesis, University of California, May, 1986.

[32] J.Y. Lee and R. Gronsky, (in preparation).

FIGURE CAPTIONS

Fig. 1a. Structure model of δ_1 phase of $Y_2Si_2O_7$ viewed in [100] orientation. Large spheres represent yttrium, medium ones silicon and small ones represent oxygen. (Output routine courtesy of W.O. Saxton).

Fig. 1b. Micrograph of δ_1 phase of $Y_2Si_2O_7$ at 1MeV and a defocus of -600Å. The insert is a simulation for a crystal 13.5nm thick.

Fig. 2a. HVEM micrograph showing precipitate-free zone near grain boundary in quench-aged Al-Ge alloy.

Fig. 2b. Needle-shaped precipitates of germanium along $\langle 100 \rangle_{Al}$ directions in quench-aged Al-Ge sample viewed along $\langle 100 \rangle_{Al}$ zone axis. The small dots are needles seen end-on.

Fig. 2c. High-resolution micrograph of germanium needle seen end-on. Note internal twinning and flat parallel faces on $\{111\}_{Ge} \,||\, \{310\}_{Al}$ planes.

Fig. 3a. Microdiffraction pattern from a small region of icosahedral phase in splat-quenched Al-25.3wt%Mn alloy. The inset convergent beam pattern exhibits the true five-fold symmetry.

Fig. 3b. Typical microstructure of splat-quenched Al-25.3wt%Mn alloy. Composition and diffraction analyses were performed on thin areas of the flower-shaped dendritic regions characteristic of the icosahedral phase.

Fig. 3c,d. Typical EDX spectra from the matrix phase (c) and the icosahedral phase (d). A counting time of 300 seconds and a count rate of 1500 cts/sec were used to ensure good statistics.

Fig. 4. [100] zone axis pattern of $MgAl_2O_4$ obtained using the pyrocatechol development process. Details of the zero-order Laue zone and a segment of the first-order Laue zone including the (1,21,1) reflections.

Fig. 5a. High resolution image of aluminum/oxide interface in a sample heat treated 0.5 hr at 600°C. The {111} planes of the Al matrix have a spacing of 0.23 nm, while the lattice planes of the crystalline oxide match with those of γ-Al_2O_3.

Fig. 5b. Twin boundaries in the oxide phase compared with simulated image (inset) at a $\Sigma = 3$ CSL orientation.

Fig. 6 HVEM micrographs taken from video recording of in-situ deformation of stainless steel sample using straining stage. Slip bands visible in (a) are advancing toward grain boundary in (b). In (c) dislocations pile up against grain boundary causing stress concentration, visible through strain contrast in neighboring grain. (Courtesy W.A.T. Clark).

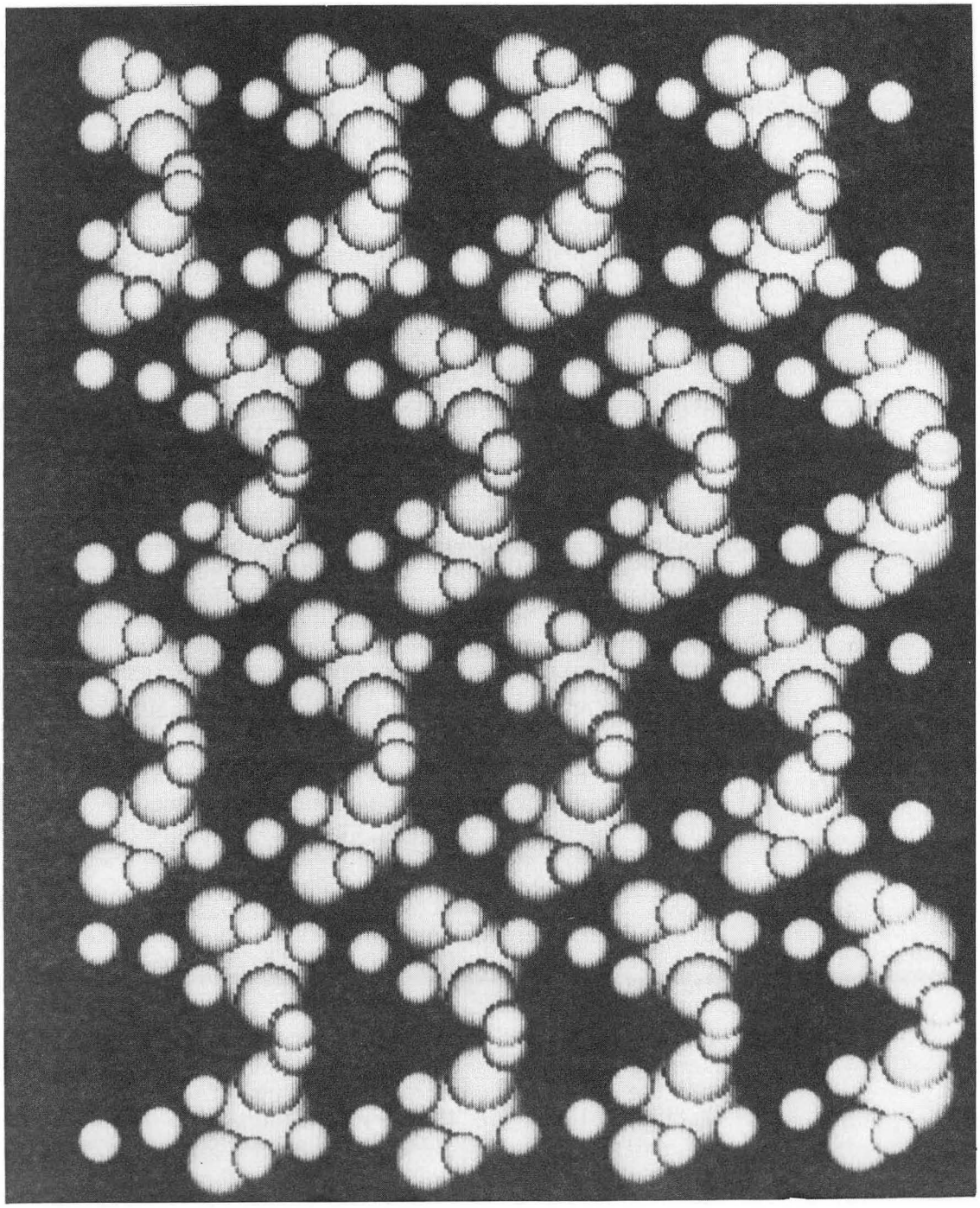

Fig. 1a

XBB 8610-8554

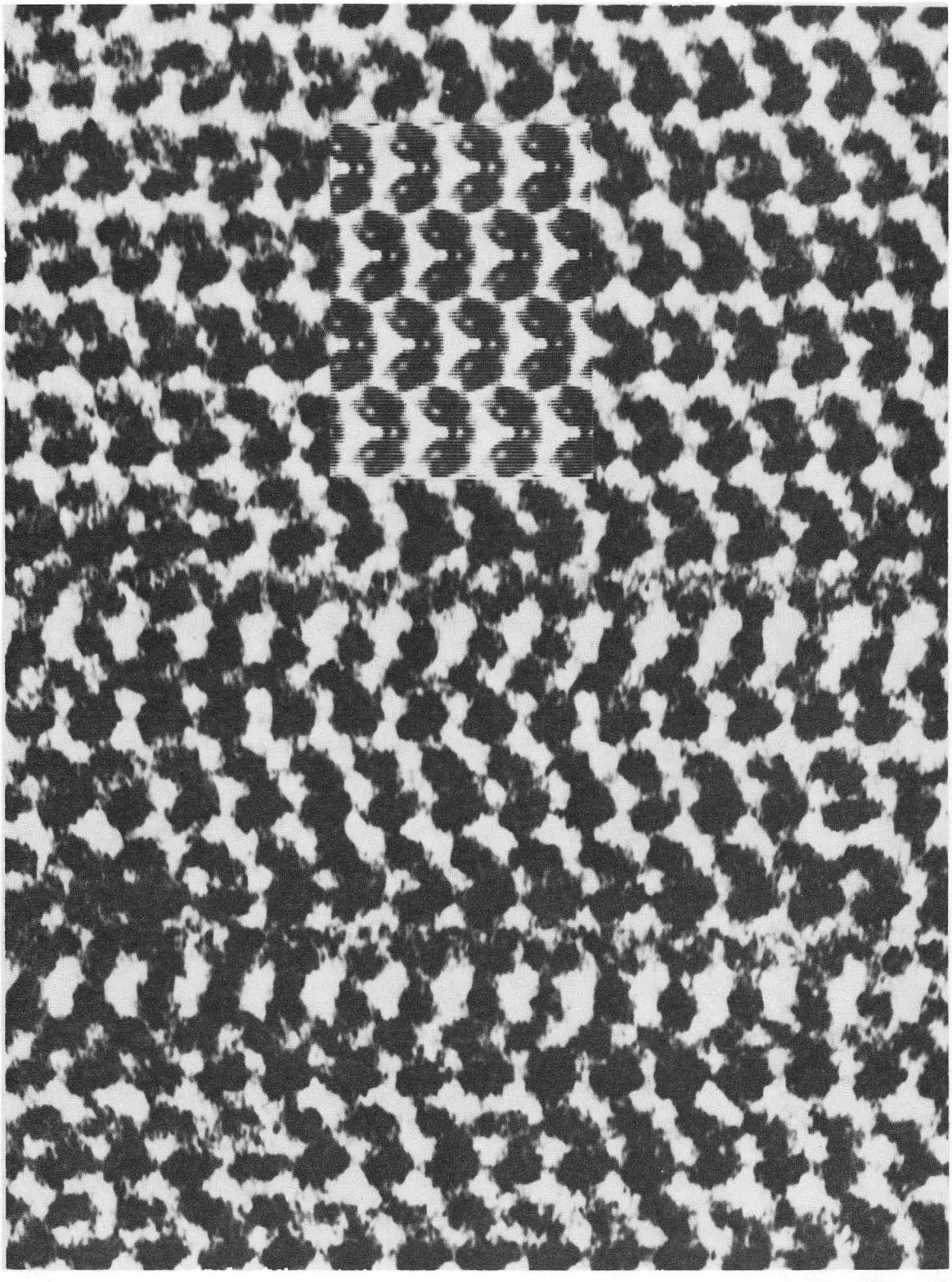

XBB 8610-804

Fig. 1b

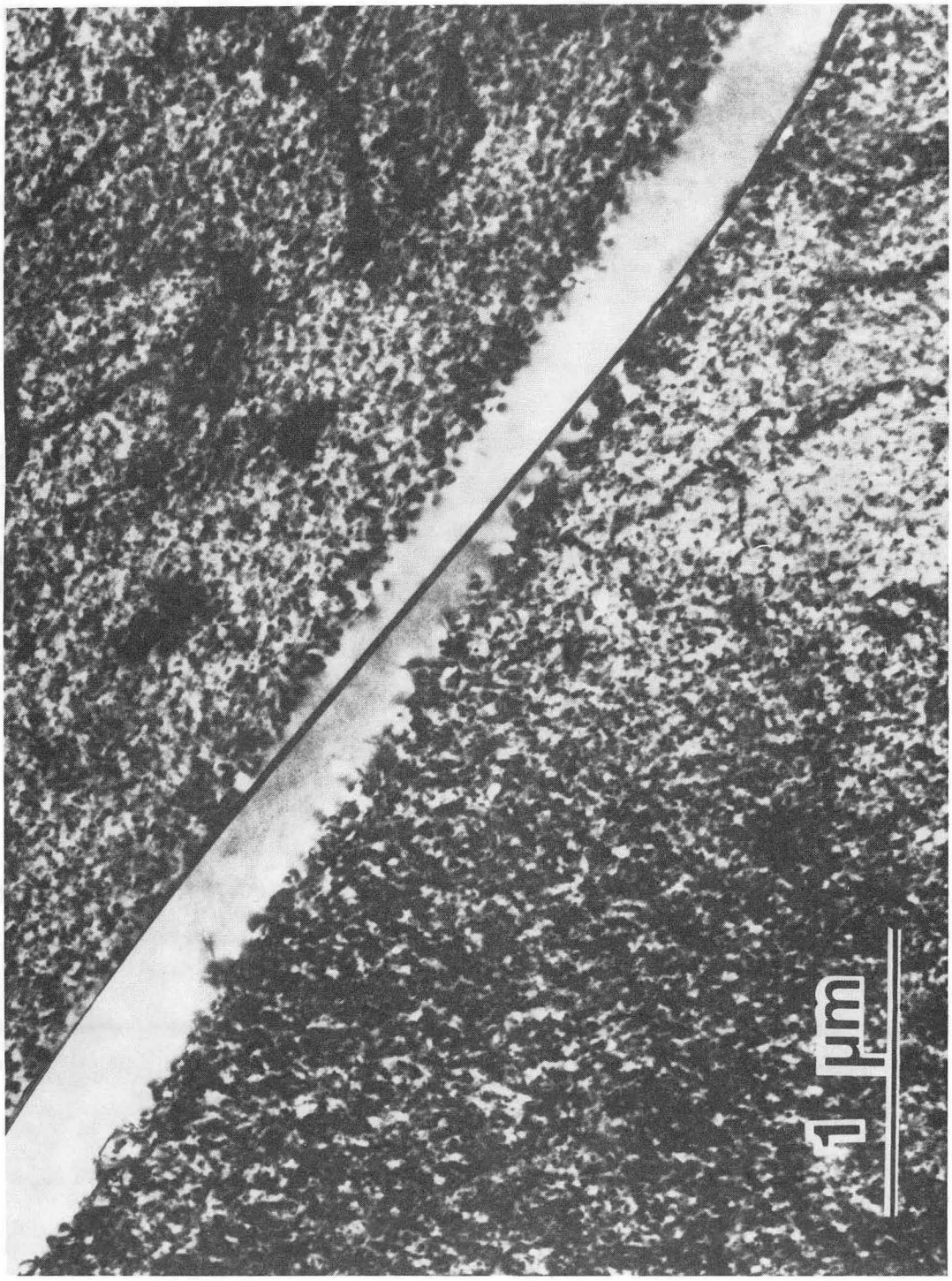

Fig. 2a

XBB 865-3757

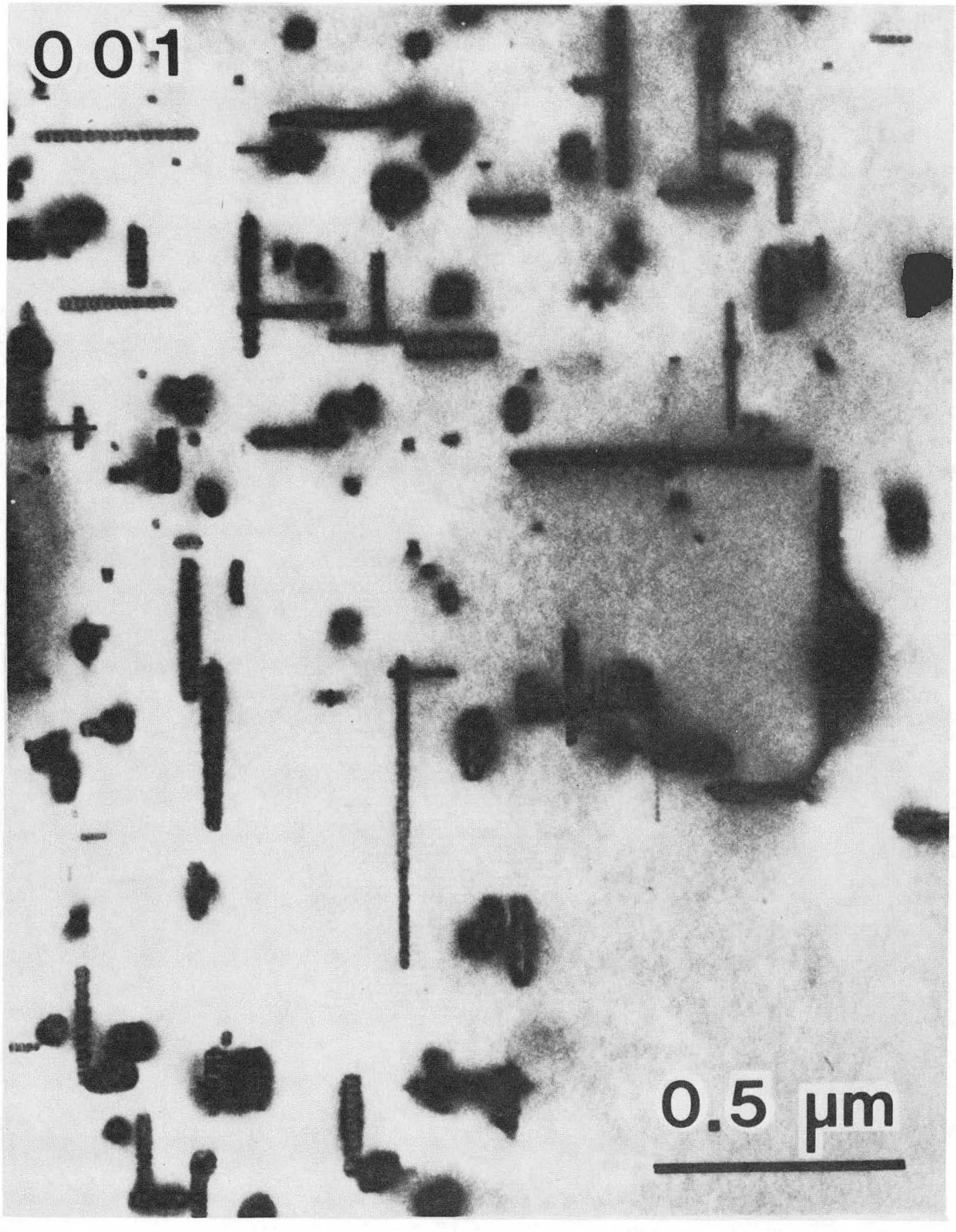

Fig. 2b

XBB 861-298

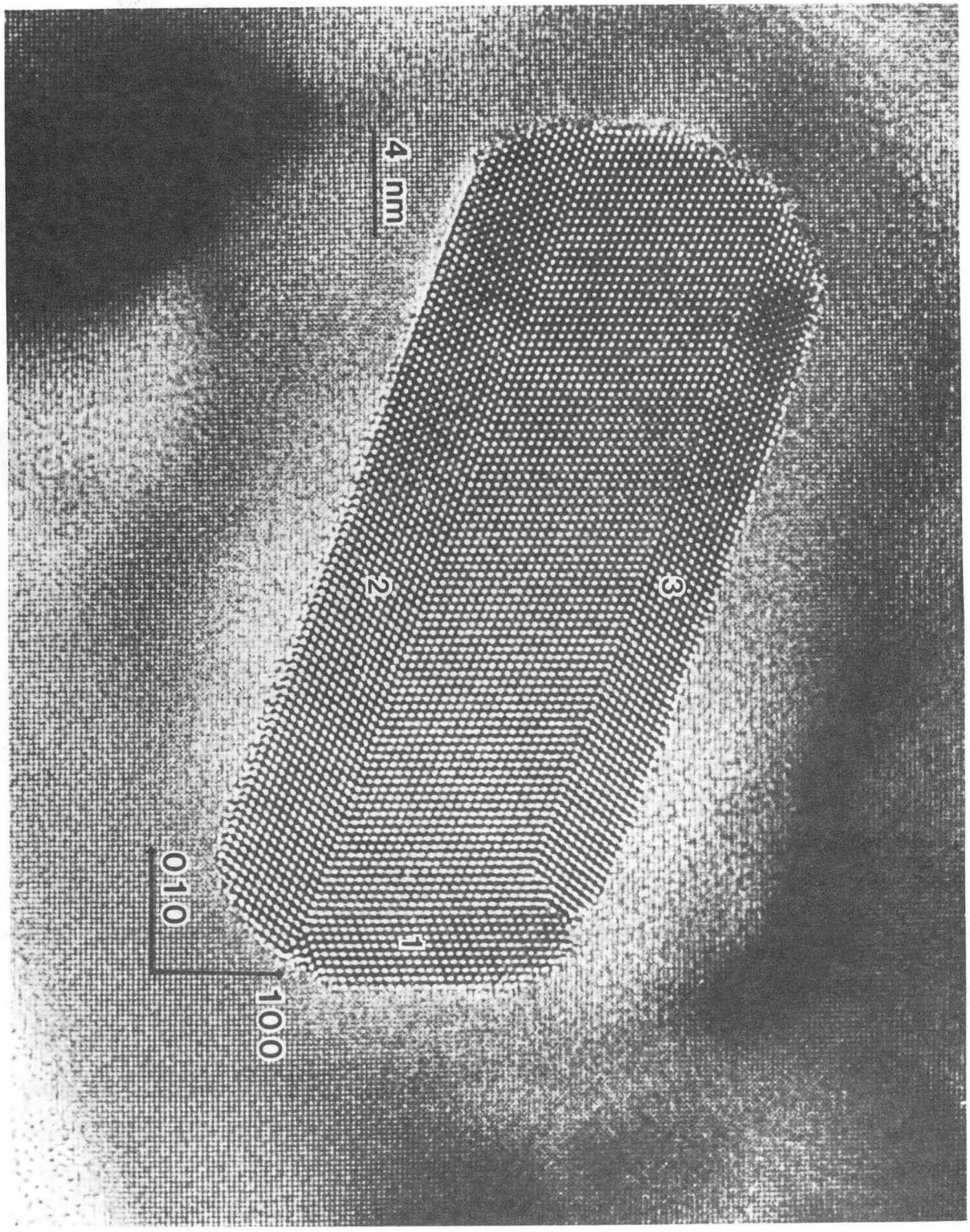

Fig. 2c

XBB 8610-8555

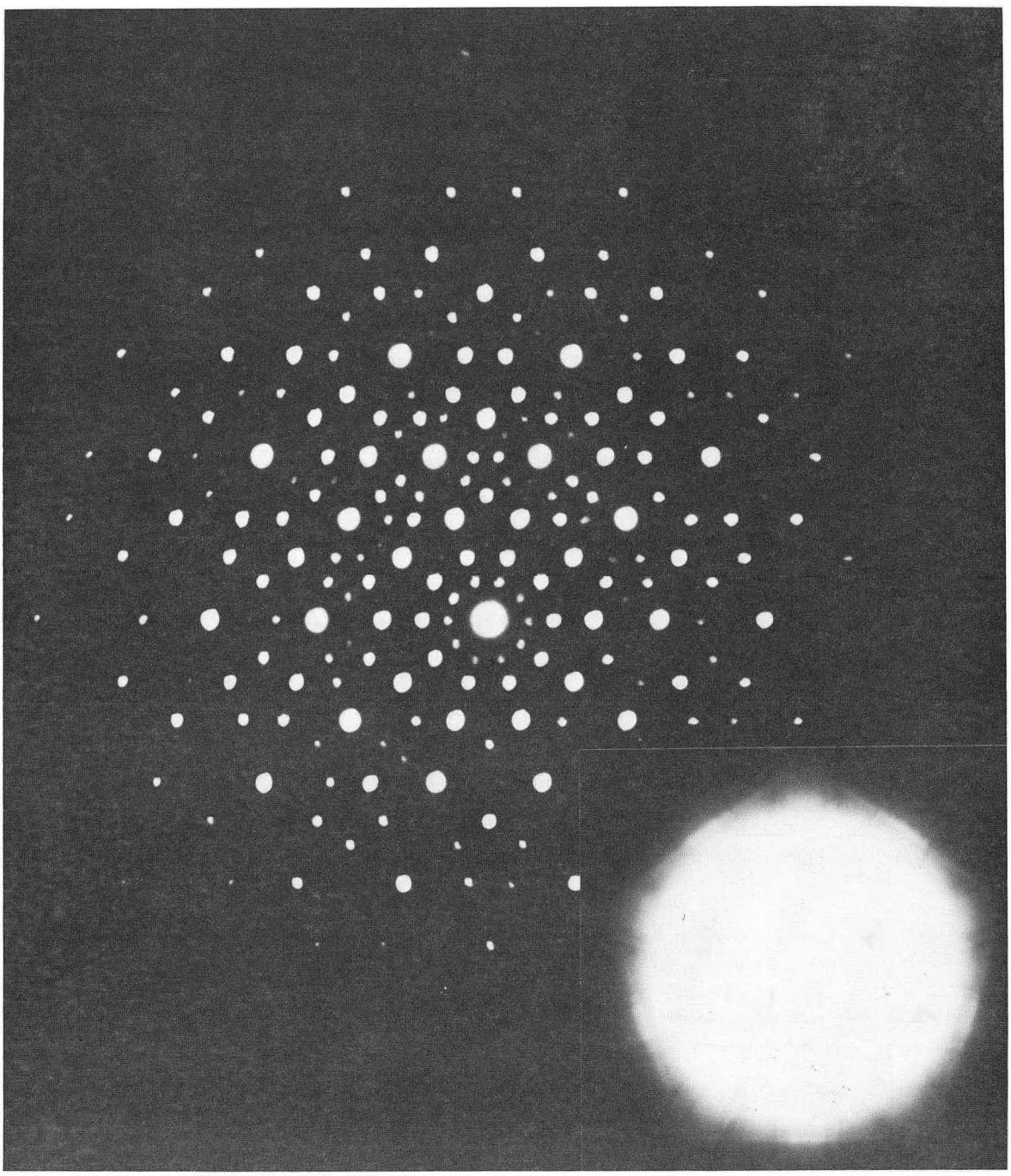

Fig. 3a

XBB 860-8552

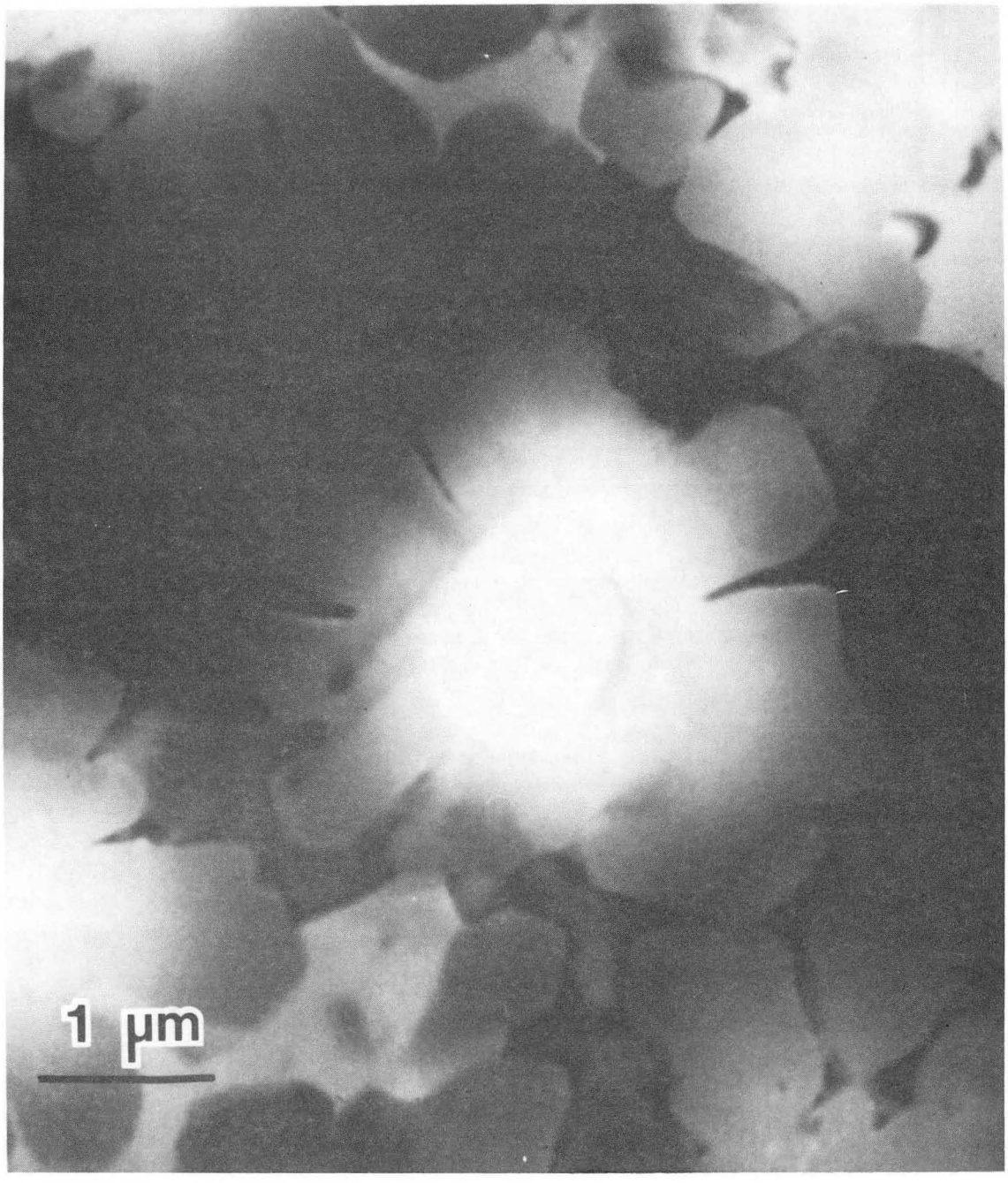

Fig. 3b XBB 860-8553

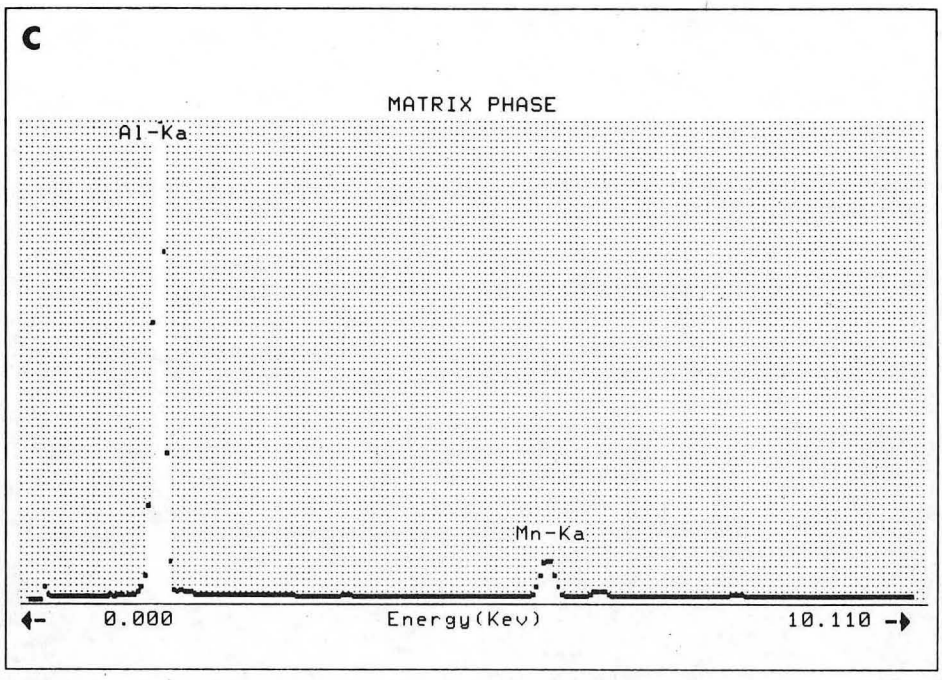

Fig. 3c

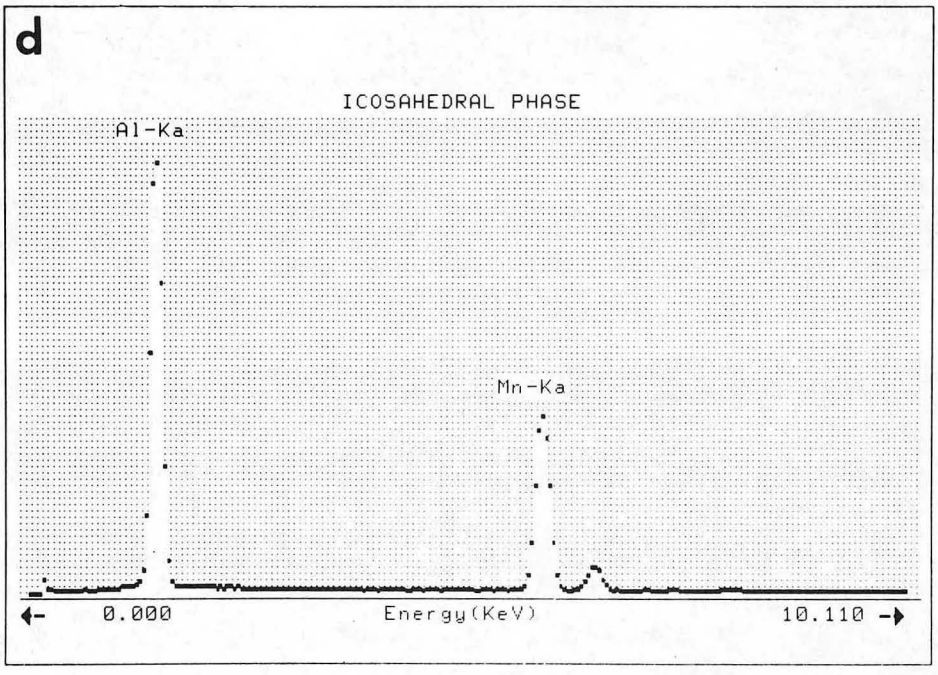

Fig. 3d

XBL 8610-3966

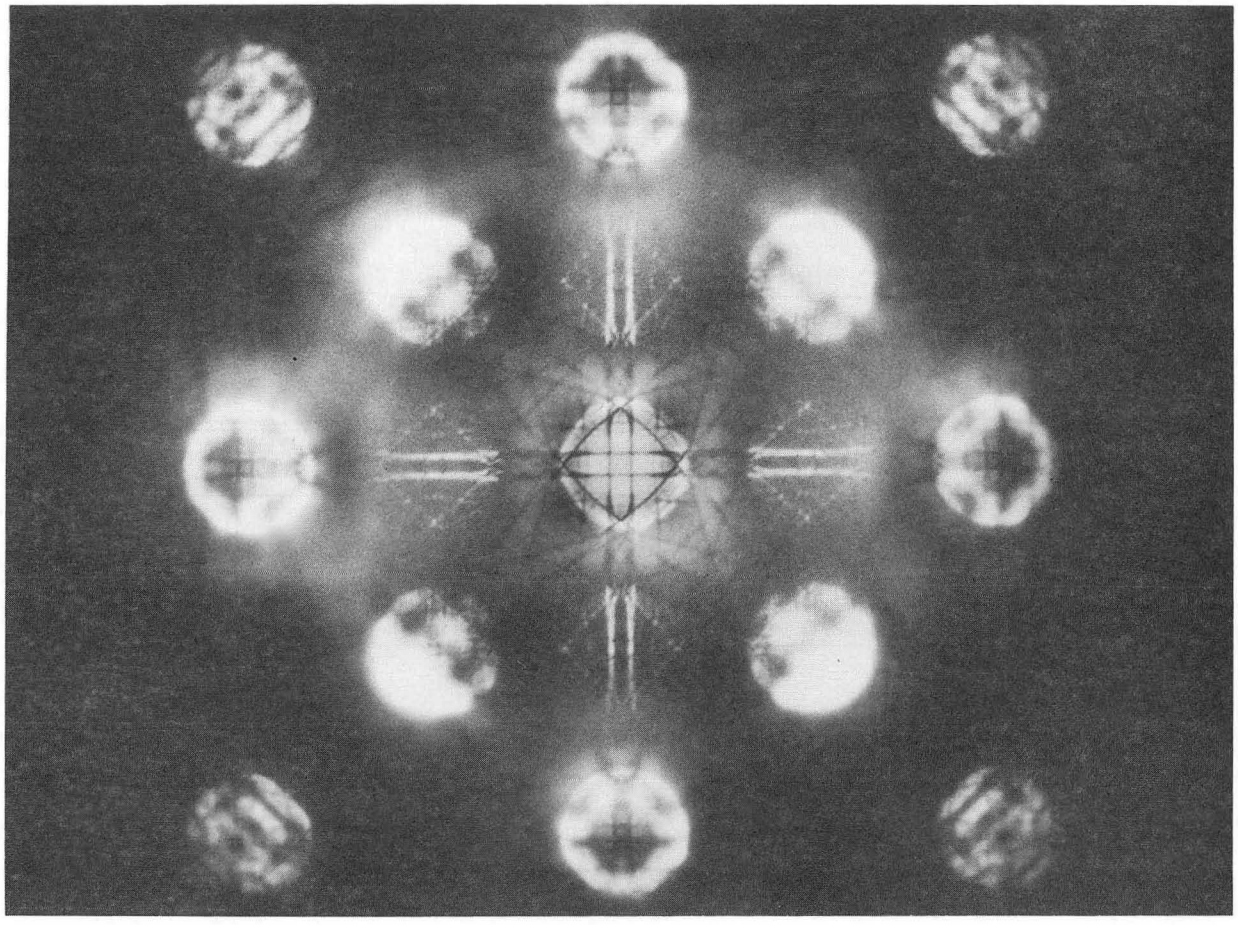

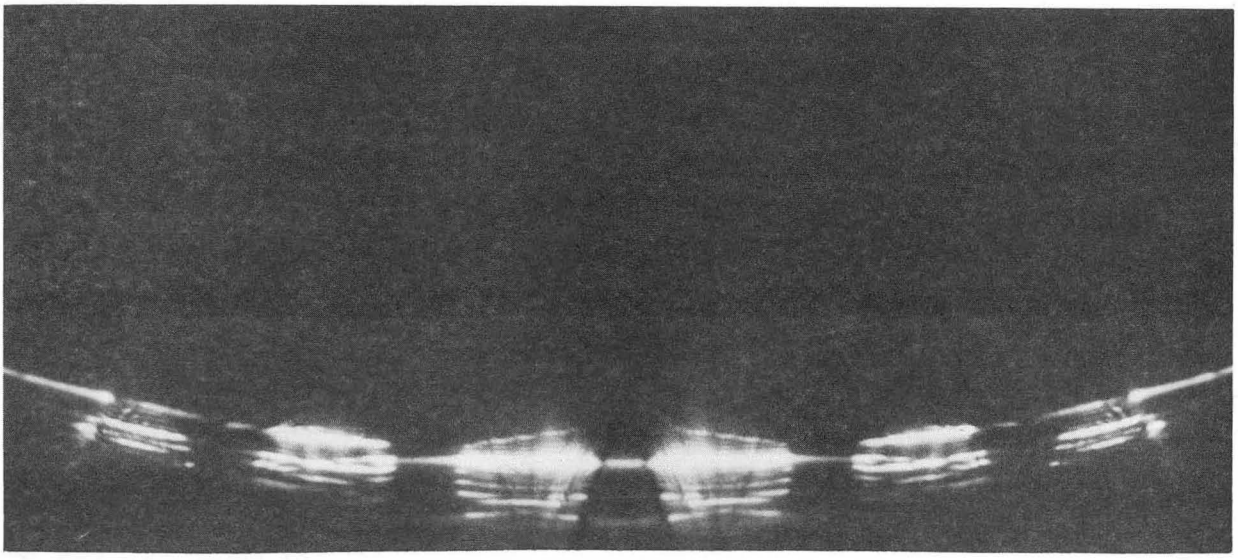

Fig. 4

XBB 864-2943

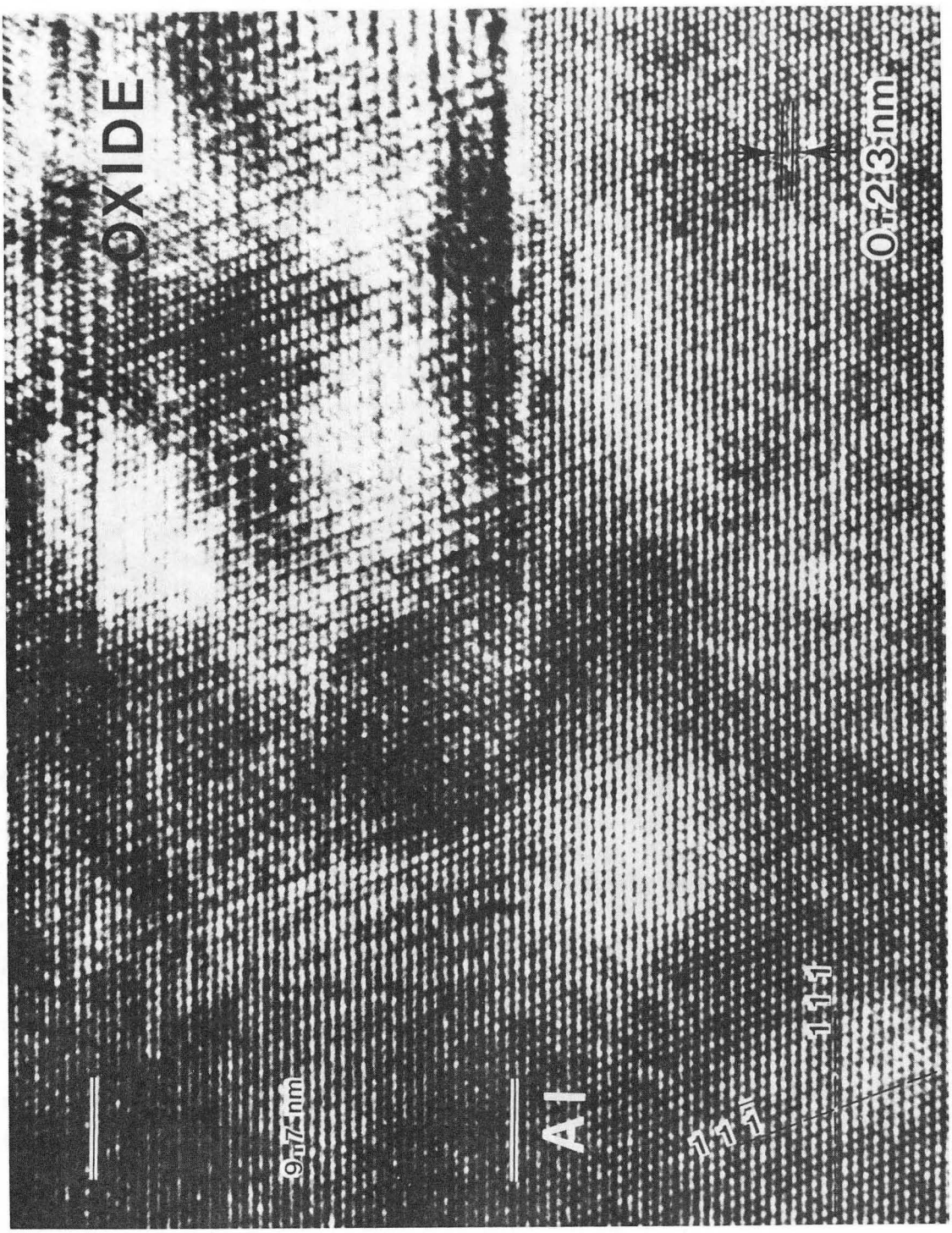

Fig. 5a

XBB 851-904

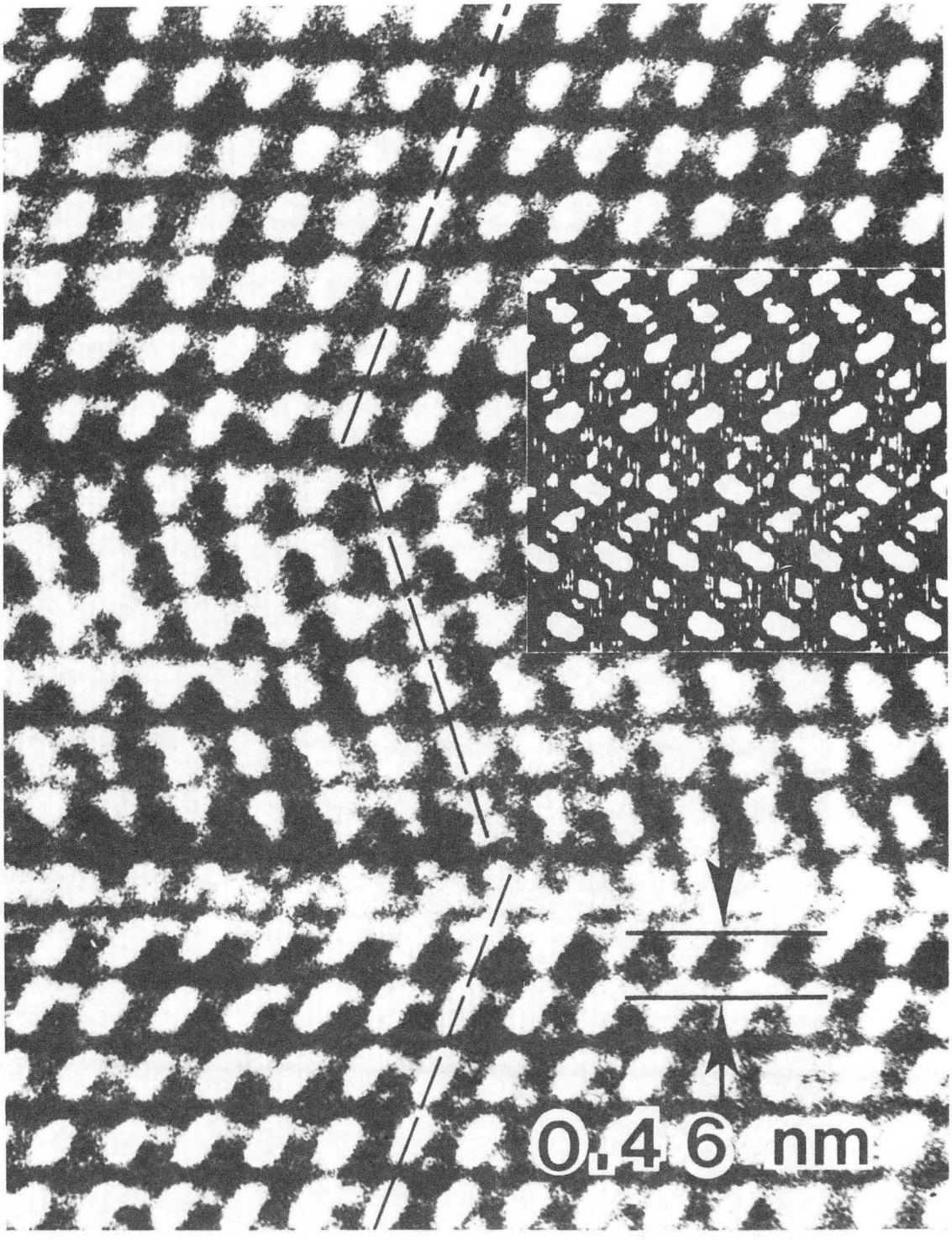

Fig. 5b XBB 852-1069

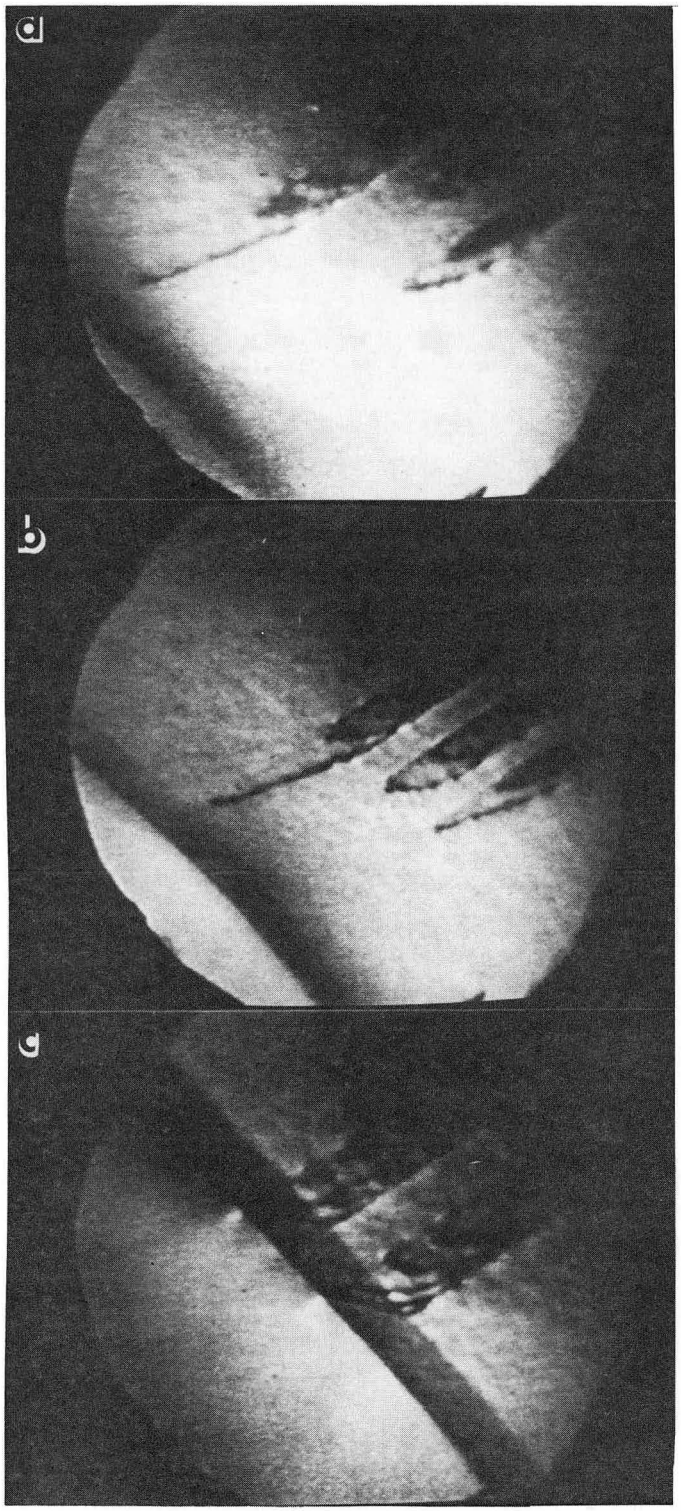

Fig. 6 XBB 8610-8556

This report was done with support from the Department of Energy. Any conclusions or opinions expressed in this report represent solely those of the author(s) and not necessarily those of The Regents of the University of California, the Lawrence Berkeley Laboratory or the Department of Energy.

Reference to a company or product name does not imply approval or recommendation of the product by the University of California or the U.S. Department of Energy to the exclusion of others that may be suitable.

LAWRENCE BERKELEY LABORATORY
TECHNICAL INFORMATION DEPARTMENT
UNIVERSITY OF CALIFORNIA
BERKELEY, CALIFORNIA 94720